



# On the Role of Arkypallidal and Prototypical Neurons for Phase Transitions in the External Pallidum

 Richard Gast,<sup>1</sup> Ruxue Gong,<sup>1</sup> Helmut Schmidt,<sup>1</sup>  Hil G.E. Meijer,<sup>2</sup> and Thomas R. Knösche<sup>1,3</sup>

<sup>1</sup>Max Planck Institute for Human Cognitive and Brain Sciences, Brain Networks Group, Leipzig, Germany 04103, <sup>2</sup>Department of Applied Mathematics, Technical Medical Centre, University of Twente, Enschede, The Netherlands 7522 NB, and <sup>3</sup>Institute for Biomedical Engineering and Informatics, Ilmenau, Germany 98684

The external pallidum (globus pallidus pars externa [GPe]) plays a central role for basal ganglia functions and dynamics and, consequently, has been included in most computational studies of the basal ganglia. These studies considered the GPe as a homogeneous neural population. However, experimental studies have shown that the GPe contains at least two distinct cell types (prototypical and arkypallidal cells). In this work, we provide *in silico* insight into how pallidal heterogeneity modulates dynamic regimes inside the GPe and how they affect the GPe response to oscillatory input. We derive a mean-field model of the GPe system from a microscopic spiking neural network of recurrently coupled prototypical and arkypallidal neurons. Using bifurcation analysis, we examine the influence of dopamine-dependent changes of intrapallidal connectivity on the GPe dynamics. We find that increased self-inhibition of prototypical cells can induce oscillations, whereas increased inhibition of prototypical cells by arkypallidal cells leads to the emergence of a bistable regime. Furthermore, we show that oscillatory input to the GPe, arriving from striatum, leads to characteristic patterns of cross-frequency coupling observed at the GPe. Based on these findings, we propose two different hypotheses of how dopamine depletion at the GPe may lead to phase-amplitude coupling between the parkinsonian beta rhythm and a GPe-intrinsic  $\gamma$  rhythm. Finally, we show that these findings generalize to realistic spiking neural networks of sparsely coupled Type I excitable GPe neurons.

**Key words:** basal ganglia; neural network; oscillations; pallidum; Parkinson; phase-amplitude coupling

## Significance Statement

Our work provides (1) insight into the theoretical implications of a dichotomous globus pallidus pars externa (GPe) organization, and (2) an exact mean-field model that allows for future investigations of the relationship between GPe spiking activity and local field potential fluctuations. We identify the major phase transitions that the GPe can undergo when subject to static or periodic input and link these phase transitions to the emergence of synchronized oscillations and cross-frequency coupling in the basal ganglia. Because of the close links between our model and experimental findings on the structure and dynamics of prototypical and arkypallidal cells, our results can be used to guide both experimental and computational studies on the role of the GPe for basal ganglia dynamics in health and disease.

## Introduction

The basal ganglia (BG) are a set of interconnected subcortical nuclei that form different feedback loops with cortex and thalamus (Alexander and Crutcher, 1990; Bolam et al., 2000). Because

of its recurrent connections with nearly all other BG nuclei, the globus pallidus pars externa (GPe) plays a major role in information transmission through the BG (Kita, 2007). In Parkinson's disease (PD), synchronized oscillations have been reported throughout all major BG nuclei (Wichmann, 2019), including the GPe (Wichmann and Soares, 2006; Mallet et al., 2008). These oscillations are characterized by transient power increases in the  $\beta$  frequency band (12–30 Hz) and an increased phase-amplitude coupling (PAC) between the phase of a  $\beta$  signal and the amplitude of a high-frequency  $\gamma$  signal (50–250 Hz) (Jenkinson et al., 2013; Lofredi et al., 2019; Gong et al., 2021). Computational models of BG phase transitions in PD suggest that the GPe is involved in the oscillation generation, either via its recurrent coupling with the subthalamic nucleus (STN) or via its processing of inputs from striatum (STR) (Pavlidis et al., 2015; Schroll and Hamker, 2016; Rubin, 2017). Most of these computational

Received Jan. 15, 2021; revised Apr. 8, 2021; accepted May 13, 2021.

Author contributions: R. Gast, H.S., H.G.E.M., and T.R.K. designed research; R. Gast, H.G.E.M., and T.R.K. performed research; R. Gast and R. Gong analyzed data; R. Gast wrote the first draft of the paper; R. Gast, R. Gong, H.S., H.G.E.M., and T.R.K. edited the paper; R. Gast wrote the paper; R. Gong contributed unpublished reagents/analytic tools.

R. Gast was supported by Studienstiftung des deutschen Volkes. H.S. was supported by German Research Foundation DFG KN 588/7-1 awarded to T.R.K. via Priority Program 2041, "Computational Connectomics." We thank Bastian Pietras and Ernest Montbrío for helpful discussions.

The authors declare no competing financial interests.

Correspondence should be addressed to Richard Gast at rgast@cbs.mpg.de.

<https://doi.org/10.1523/JNEUROSCI.0094-21.2021>

Copyright © 2021 the authors

models regarded the GPe as a homogeneous population of neurons. However, two major cell types have been identified within the GPe, which differ in their electrophysiological properties, firing rates, and firing patterns: prototypical (GPe-p) and arky pallidal (GPe-a) cells (Cooper and Stanford, 2000; Abdi et al., 2015; Hegeman et al., 2016). Regarding their efferent synapses, it has been shown that GPe-p cells preferentially project to subthalamic nucleus (STN) and BG output nuclei, whereas GPe-a cells provide feedback to striatum (STR) (Mallet et al., 2012; Hernández et al., 2015; Fujiyama et al., 2016). Furthermore, recent studies found that STN and STR differentially affect GPe-p and GPe-a in mice (Pamukcu et al., 2020; Ketzef and Silberberg, 2021). Regarding cell type-specific differences in GPe-intrinsic axon collaterals, there is evidence from mice experiments that prototypical cells express more numerous axon collaterals than arky pallidal cells (Mallet et al., 2012; Higgs et al., 2021; Ketzef and Silberberg, 2021). Still, a substantial number of arky pallidal axon collaterals was identified that targeted prototypical GPe cells (Mallet et al., 2012).

Depending on the pattern of mutual inhibition between those two major GPe cell populations, different modes of GPe internal dynamics may exist. Asymmetric connections between the two cell types may give rise to a feedforward inhibition scenario, where an excitatory input to one population could silence the other population. Alternatively, winner-takes-all (WTA) dynamics can arise in scenarios of mutual inhibition between two populations (Schmidt et al., 2018). Either of these two scenarios could explain the recent findings from optogenetic stimulation in mice, where silencing the GPe-p led to increased GPe-a firing (Aristieta et al., 2021). The same work suggests that STN and STR express asymmetric projections to GPe-p versus GPe-a that allow for transient switching between the two different output pathways of the GPe. To be able to infer the neurodynamic mechanism underlying such data, we argue for an improved understanding of the relationship between synaptic coupling and neural dynamics in a GPe composed of arky pallidal and prototypical cells. Whereas some computational models have considered the role of arky pallidal feedback to STR (Nevado-Holgado et al., 2014; Corbit et al., 2016; Je, drzejewski-Szmek et al., 2018), a neurodynamic understanding of the structure-function relationships inside a dichotomous GPe is still missing. In this study, we examine the effects of GPe coupling patterns on GPe behavior. For this purpose, we derive and analyze a mean-field description of two fully coupled inhibitory populations, following the approach by Luke et al. (2013) and Montbrió et al. (2015). Importantly, this mean-field description captures the exact macroscopic dynamics of the underlying, heterogeneous spiking neural network and can thus capture population-intrinsic spike resonance phenomena that classic mean-field approaches would miss. This in itself makes our modeling approach interesting for the understanding of synchronization processes inside the GPe. Using bifurcation analysis of the two-population GPe model, we identify monostable, bistable, and oscillatory regimes, the existence of which depends on the GPe-intrinsic coupling pattern. We then show that the GPe expresses distinct responses to periodic input when initialized in either of these regimes. Finally, we analyze how the macroscopic phase transitions found in the GPe mean-field model translate to spiking neural networks with realistic numbers of neurons and axons.

## Materials and Methods

### Model definition

**Mathematical formulation of population dynamics.** We consider the GPe as a nucleus of two distinct populations of GABAergic projection

neurons (Kita, 2007; Hegeman et al., 2016). Whereas prototypical neurons express high average spontaneous firing rates of 50–70 Hz (DeLong, 1971; Wichmann and Soares, 2006; Jaeger and Kita, 2011), arky pallidal neurons fire with considerably reduced average firing rates of 5–15 Hz (Abdi et al., 2015; Dodson et al., 2015; Hernández et al., 2015; Aristieta et al., 2021). To model synaptic influences on the spike timings of GPe neurons, it is important to know their type of excitability. This can be inferred from their phase-response curve (Gutkin et al., 2005). Neurons can either express Type I excitability, meaning that the direction in which the excitability of a neuron is changed by extrinsic input is not dependent on the intrinsic phase of the neuron, or express Type II excitability, meaning that the direction in which the excitability of a neuron is changed by extrinsic input does depend on the intrinsic phase of the neuron (Izhikevich, 2000). While computational studies demonstrated that both Type I and Type II excitability can be identified in single-cell models of GPe neurons (Schultheiss et al., 2010; Fujita et al., 2012), experimental investigations only revealed Type I excitability so far (Wilson, 2013). Furthermore, it has been shown that coupled networks of Type I excitable neurons can express Type II excitability on the network level (Dumont and Gutkin, 2019). Thus, as a base neuron model, we use the quadratic integrate-and-fire neuron (QIF), which is the canonical form of Type I excitable neurons and expresses a quadratic and thus nonlinear input-output relationship (Izhikevich, 2000). This choice also accounts for the nonlinear input-output relationship reported in prototypical and arky pallidal cells (Kita, 2007; Abdi et al., 2015). The evolution equation of the  $j^{\text{th}}$  QIF neuron embedded within either the GPe-p or GPe-a is given by the following:

$$\tau \dot{V}_j = V_j^2 + \eta_j + I(t) + Jm\tau, \quad (1)$$

$$m = \frac{1}{N} \sum_{i=1}^N \sum_{k: t_i^k < t} \int_{-\infty}^t g(t-t') \delta(t'-t_i^k) dt', \quad (2)$$

with neural excitability  $\eta_j$ , synaptic strength  $J$ , evolution time constant  $\tau$ , extrinsic input  $I(t)$ , and synaptic activation  $m$ . A neuron  $j$  generates its  $k^{\text{th}}$  spike at time  $t_i^k$ . At this time, it reaches the spiking threshold  $V_\theta$  and the membrane potential  $V_j$  is reset to a reset potential  $V_r$ . The integral kernel  $g(t-t')$  represents synaptic dynamics, for example, in the case of mono-exponential synapses  $g(t) = e^{-t/\tau_m}/\tau_m$  with synaptic time scale  $\tau_m$ . We introduce the exact shape and timescales of  $g$  in the following subsection. Equations 1 and 2 represent an all-to-all coupled network of  $N$  QIF neurons with homogeneous connection strengths  $J$ . Assuming all-to-all connectivity as well as infinitely large neural populations, we can use the mean-field model proposed by Montbrió et al. (2015). The authors derived a set of two coupled differential equations describing the evolution of the macroscopic firing rate  $r$  and membrane potential  $v$  of the QIF population given by Equations 1 and 2 as follows:

$$\tau \dot{r} = \frac{\Delta}{\pi\tau} + 2rv, \quad (3)$$

$$\tau \dot{v} = v^2 + \eta + I(t) + Jm\tau - (\pi r\tau)^2, \quad (4)$$

$$m = \int_{-\infty}^t g(t-t') r(t') dt' = r \otimes g. \quad (5)$$

Here, the synaptic activation  $m$  takes the form of a simple convolution of the average firing rate  $r$  with the synaptic response kernel  $g$ , henceforth abbreviated by the convolution operator  $\otimes$ . The parameters  $\eta$  and  $\Delta$  are the center and half-width at half-maximum of a Lorentzian distribution over the single-neuron parameters  $\eta_j$ . Thus,  $\eta$  and  $\Delta$  allow to control the average and heterogeneity of the firing rates inside the QIF population, respectively. Spontaneous firing rates of GPe cells cannot be explained by glutamatergic input alone, since brain slice recordings still showed autonomous activity of up to 26 Hz after synaptic transmission was blocked

pharmacologically (Günay et al., 2008). In other words, GPe cells are strong pacemaker cells that show regular firing at a cell-specific frequency under synaptic isolation (Mercer et al., 2007; Abrahao et al., 2017). Across GPe cells, a substantial amount of heterogeneity of the intrinsic firing frequencies has been reported (Wilson, 2013). By considering the background excitabilities  $\eta_j$  as distributed quantities, we account for these findings.

We are aware that the all-to-all coupling and infinite population sizes are in contrast to the actual GPe structure (Wilson, 2013; Hegeman et al., 2016). However, it has been recently shown that the mean-field model predictions can generalize to a fairly wide range of network sizes and coupling probabilities (Gast et al., 2020). Even for QIF networks with recurrent coupling probabilities of 1%, the authors found that population sizes of  $N=8000$  neurons were sufficient to reproduce the macroscopic dynamics predicted by the mean-field model accurately. Given that population sizes of primate GPe are on the order of  $10^5$  and recurrent coupling probabilities are  $\sim 5\%$  (Wilson, 2013), we expect that this mean-field model is sufficient to capture the macroscopic dynamics of QIF populations with realistic cell counts and coupling probabilities.

**Mathematical formulation of axonal propagation and synaptic dynamics.** In a next step, we define the coupling function  $g$  which, in our model, acts as a lumped representation of axonal propagation and synaptodendritic integration. In other words,  $g$  serves to link single spikes emitted by neuron  $j$  to changes in the membrane potential of any other neuron. GPe to GPe connections have been suggested to express axonal transmission delays of  $\sim 1.0$  ms (Jaeger and Kita, 2011) and make use of GABAergic synapses (Kita, 2007). Since axon collaterals can express a substantial variability in individual axon diameters and myelination properties (Schmidt and Knösche, 2019), we modeled the axonal transmission delays via  $\gamma$  distributions (Smith, 2011). The probability density function of the  $\gamma$  distribution can be written as follows:

$$g(\kappa, \beta, t) = \frac{\kappa^\beta t^{\beta-1} e^{-\kappa t}}{(\beta-1)!}, \quad (6)$$

with shape parameter  $\beta$  and scale parameter  $\kappa$ . These parameters can be used to control the mean  $\mu$  and width  $\sigma$  of the delay distribution via the functional relationships  $\mu = \frac{\beta}{\kappa}$  and  $\sigma^2 = \frac{\beta}{\kappa^2}$  (Smith, 2011). Choosing Equation 6 as functional form of the function  $g$  in Equation 5, the synaptic convolution operation can be approximated by the following set of coupled ordinary differential equations (ODEs):

$$\dot{m}_i = \kappa(m_{i-1} - m_i), \quad (7)$$

where  $i = 0, 1, 2, \dots, \beta$  and  $m_0 = r$  (Smith, 2011). Using this formulation, the number of coupled ODEs depends on the shape parameter of the  $\gamma$  function, which means that the overall dimensionality of the system depends on the order parameters  $\beta$  at each synaptic connection in the model.

In addition to the axonal delays, we also included a dynamic model of the electrochemical processes that lead to a change in the postsynaptic potential after a presynaptic action potential traveled down the axon. A popular choice to express these dynamics is via a convolution with a biexponential synaptic response kernel, for which the rise and decay time constants are specific to the type of presynapse and postsynapse (Deco et al., 2008). Such a biexponential synaptic response function is given by the following:

$$z(\tau_r, \tau_d, t) = \frac{\tau_r \tau_d}{\tau_r + \tau_d} (e^{-\frac{t}{\tau_r}} - e^{-\frac{t}{\tau_d}}), \quad (8)$$

with  $\tau_r$  and  $\tau_d$ , denoting the synaptic rise and decay time constants, respectively. A convolution of the delayed axonal response  $m_\beta$  with

Equation 8 can be approximated by two coupled ODEs of the following form:

$$\dot{m} = x, \quad (9)$$

$$\dot{x} = \frac{1}{\tau_r \tau_d} (m_\beta - x(\tau_r + \tau_d) - m), \quad (10)$$

with  $m$  being the final synaptic input entering into Equation 3. Thus, we specify the convolution integral expressed by Equation 5 in our model as subsequent convolutions of  $r$  with the  $\gamma$  function (Eq. 6) and the biexponential function (Eq. 8), allowing us to capture the characteristics of both axonal delay distribution and postsynaptic currents.

**Specification of the two-population GPe model.** Based on these dynamic equations for neural populations and synaptic transmission, we can now introduce the full set of equations of our GPe model. Since the number of equations of the ODE approximation (Eq. 7) to the  $\gamma$  kernel convolution (Eq. 5) depends on the parameter  $\beta$  of (Eq. 6), we chose to provide a set of integro-differential equations for generality and brevity. However, for our results, each  $\gamma$  kernel convolution was formulated as a set of coupled ODEs of the form (Eq. 7) and each convolution with a synaptic response kernel of the form (Eq. 8) was formulated as the ODE system given by Equations 9 and 10. The following set of coupled integro-differential equations describes the average firing rate and average membrane potential dynamics at GPe-p and GPe-a as follows:

$$\tau_p \dot{r}_p = \frac{\Delta_p}{\pi \tau_p} + 2r_p v_p, \quad (11)$$

$$\tau_p \dot{v}_p = v_p^2 + \eta_p + I_p(t) - (J_{pa} m_{pa} + J_{pp} m_{pp} + J_{pe} r_e - J_{ps} r_s) \tau_p - (\pi r_p \tau_p)^2, \quad (12)$$

$$\tau_a \dot{r}_a = \frac{\Delta_a}{\pi \tau_a} + 2r_a v_a, \quad (13)$$

$$\tau_a \dot{v}_a = v_a^2 + \eta_a + I_a(t) - (J_{ap} m_{ap} + J_{aa} m_{aa} + J_{ae} r_e - J_{as} r_s) \tau_a - (\pi r_a \tau_a)^2, \quad (14)$$

where  $p$  and  $a$  are the subscripts for prototypical and arkypallidal GPe, respectively, and subscripts of the form  $A_{xy}$  represent the variable  $A$  that is specific to the synaptic transmission from population  $y$  to population  $x$ . Hence, each synaptic response function  $g_{xy}$  is specific to a given synaptic transmission and takes the following form:

$$m_{xy} = z(\tau_r^{xy}, \tau_d^{xy}, t) \otimes g(\kappa_{xy}, \beta_{xy}, t) \otimes r_y(t) \quad (15)$$

with connection specific synaptic rise and decay times  $\tau_r^{xy}$  and  $\tau_d^{xy}$  and connection-specific axonal delay distribution shape and scaling  $\kappa_{xy}$  and  $\beta_{xy}$ . Finally, we added inputs from STN and STR to the model. These can affect GPe dynamics via their constant steady-state firing rates  $r_e$  and  $r_s$ , which are again scaled by population specific connectivity constants  $J_{xy}$ .

**Mathematical formulation of extrinsic model inputs.** Extrinsic input can generally be applied via the extrinsic forcing parameters  $I_p(t)$  and  $I_a(t)$  to GPe-p and GPe-a, respectively. In our simulations, we applied step function inputs to each of the populations. These are defined as follows:

$$I_x(t) = \begin{cases} \alpha, & \text{if } t_{\text{start}} < t < t_{\text{end}} \\ 0, & \text{otherwise.} \end{cases} \quad (16)$$

Here,  $\alpha$  defines the input strength, whereas  $t_{\text{start}}$  and  $t_{\text{end}}$  define the beginning and end of the time interval in which the input is applied. Furthermore, we also applied periodic input to the GPe-p, since the

GPe-p seems to be most strongly affected by subthalamopallidal and striatopallidal inputs (Aristieta et al., 2021). We used the Stuart-Landau oscillator as the generating model of a sinusoidal signal with period  $\omega$  (Fujimura, 1997) as follows:

$$\dot{X} = -\frac{2\pi Y}{\omega} + X(1 - X^2 - Y^2), \quad (17)$$

$$\dot{Y} = \frac{2\pi X}{\omega} + Y(1 - X^2 - Y^2). \quad (18)$$

Additionally, to account for the bursting characteristics of typical striatal inputs arriving at the GPe (Jaeger et al., 1995), we applied a sigmoidal transformation to the Stuart-Landau oscillator, giving us the final input as follows:

$$I_p(t) = S(X(t), \alpha, \gamma, \omega, t_{on}) * z(\tau_r, \tau_d, t), \quad (19)$$

$$S(X, \alpha, \gamma, \omega, t_{on}) = \frac{\alpha}{1.0 + e^{-\gamma \left( X - \cos\left(\frac{2\pi t_{on}}{\omega}\right) \right)}}, \quad (20)$$

where  $S$  represents a sigmoidal transform with maximum  $\alpha$  and steepness  $\gamma$ . The cosine term ensures that the input  $I_p(t)$  only expresses bursts around the maxima of  $X$ . We set the steepness of the bursts to  $\gamma = 100.0$  and the width of the bursts to  $t_{on} = 5.0$  ms. For a more detailed description of this sigmoidal transformation of a sinusoidal signal to a periodic square wave, see Lourens et al. (2015). Finally, the result of the sigmoidal transform is convoluted with a bi-exponential synaptic kernel, where the rise and decay times are chosen as  $\tau_r = 0.5$  and  $\tau_d = 5.0$ , thus accounting for the time constants of GABAergic synapses reported in the GPe (Sims et al., 2008). This way, the final input  $I_p(t)$  reflects burst-like striatal input that enters at GPe neurons via GABAergic synapses.

#### Model analysis

To analyze the behavior of the model given by Equations 11–14, we used the open-source Python toolbox PyRates (Gast et al., 2019). We chose PyRates' interface to the SciPy Runge-Kutta solver with adaptive integration step-size (Virtanen et al., 2020) for numerical integration of the model dynamics for a given initial condition. For bifurcation analysis, we used PyRates' interface to Auto-07p (Doedel et al., 2007) to perform numerical parameter continuation and automatic bifurcation detection (for an in-depth explanation of these techniques, see Kuznetsov, 2004; Meijer et al., 2009). To analyze the behavior of the spiking neural networks corresponding to our mean-field models, we used custom MATLAB code. Numerical integration of the spiking neural network dynamics was performed via an explicit Euler algorithm with an integration step-size of 0.001 ms, which we found to be sufficiently small to capture all model dynamics. The scripts and configuration files for all simulations and parameter continuations are available at the following public Github repository: [https://github.com/Richert/GPe\\_Dynamics](https://github.com/Richert/GPe_Dynamics).

#### Spectral analysis

We also analyzed the GPe model behavior in the frequency domain. To this end, we used time series of 320 s of simulated GPe-p firing rate dynamics sampled at 1 ms and cut off the first 20 s to remove initial transients from the time series. Power spectral densities were calculated from the raw simulation data using Welch's method. We used FFT segments of length 2048 and an overlap between segments of 1024 time steps. For quantification of PAC and phase-phase coupling (PPC) between different frequency components of the GPe-p firing rate dynamics, we followed the procedure described by Gong et al. (2021). PAC measures the amount of modulation of the amplitude of a high-frequency signal by the phase of a low-frequency signal and was evaluated by means of the Kullback-Leibler-based modulation index (KL-MI) (Tort et al., 2010). Both the low- and high-frequency signals were acquired by bandpass filtering the GPe-p firing rate time series. Following the procedure described by Gong et al. (2021), we evaluated the KL-MI for multiple

pairs of phases at frequencies  $f_p \in 2, 4, 6, \dots, 30$  Hz and amplitudes at frequencies  $f_a \in 50, 60, 70, \dots, 250$  Hz. For each pair of  $f_p$  and  $f_a$ , we filtered the GPe-p firing rate using an FIR bandpass filter centered at  $f_p$  with a bandwidth of 2 Hz and using another FIR bandpass centered at  $f_a$  with a bandwidth of  $f_p$  Hz. We then applied the Hilbert transform to the two bandpass filtered signals and extracted the phase from the signal filtered around  $f_p$  and the amplitude of the signal filtered around  $f_a$ . Phases were then sorted into 16 bins, and the amplitudes corresponding to each bin were averaged. Then, the KL-MI of the distribution of the average amplitude across phase bins was calculated as described by Tort et al. (2010), which measures the difference to a uniform distribution. Furthermore, we evaluated PPC for the GPe-p firing rates filtered around  $f_p$  and  $f_a$  using the waveform analysis described by Gong et al. (2021). In short, this method calculates the average waveform of the high-frequency signal, time-locked to the zero-crossing of the low-frequency signal. The resulting metric is bounded between 0 and 1, with PPC = 1 indicating that the phase of the high-frequency signal (filtered at  $f_a$ ) is always the same at zero-crossings of the phase of the low-frequency signal (filtered at  $f_p$ ). Hence, for a given GPe-p firing rate time series, we acquired a  $15 \times 21$  PAC (PPC) matrix  $C_{pa}$  ( $C_{pp}$ ) with entries for each pair of  $f_a$  and  $f_p$ . To evaluate the overall amount of PAC in a time series, we calculated the average across the PAC matrix (mean PAC in Fig. 4). To evaluate the similarity between PAC and PPC across low- and high-frequency components of a time series, we calculated the Pearson correlation coefficient between the PAC and the PPC matrix (PAC-PPC correlation in Fig. 4).

#### Model parameters

The dynamics at GPe-p and GPe-a are each governed by membrane time constants  $\tau$  and two parameters  $\eta$  and  $\Delta$  that determine the center and half-width at half-maximum of the distribution of single-cell firing rates inside the populations. Additionally, the four synaptic connections between GPe-p and GPe-a are each parameterized via a lumped synaptic strength  $J$ , two axonal delay parameters  $\mu$  and  $\sigma$ , and the synaptic rise and decay time constants  $\tau_r$  and  $\tau_d$ . For all model analysis, we used rescaled synaptic strength parameters  $k = \frac{J}{10}$ . To find a parameterization of the model that resembles realistic macroscopic neural dynamics inside the GPe, we imposed the following conditions for the model behavior: (1) The input-output relationship of isolated GPe-p and GPe-a QIF neurons should qualitatively replicate the data reported by Abdi et al. (2015). (2) The distribution of single-cell firing rates in the GPe-p and GPe-a populations should qualitatively resemble the data reported previously (Kita et al., 2004; Miguez et al., 2012; Aristieta et al., 2021; Ketzef and Silberberg, 2021). (3) The average firing rates of GPe-p and GPe-a neurons should behave as reported previously (Kita et al., 2004; Wichmann and Soares, 2006; Aristieta et al., 2021) under control conditions as well as conditions of striatal stimulation, subthalamic inhibition, or blockade of AMPA/GABAA transmission. By hand-tuning our model, we found the parameter set reported in Table 1 to meet these conditions well. We provided references for parameters that were additionally constrained by the literature. If not reported otherwise, model parameters were set to these default values. As can be seen in Figure 1A, our model replicates the findings that GPe-p neurons express more heterogeneous firing rates than GPe-a neurons, whereas GPe-a includes a larger number of silent neurons than GPe-p (Dodson et al., 2015; Aristieta et al., 2021). Furthermore, the I-f curves shown for GPe-p and GPe-a populations and single cells in Figure 1B agree with the data by Abdi et al. (2015). Finally, Figure 1C shows that the model responses to extrinsic manipulation of inputs and synaptic strengths of the GPe populations match the experimental results reported previously (Kita et al., 2004; Wichmann and Soares, 2006; Aristieta et al., 2021).

## Results

In this section, we report the results of our analysis of the relationship between model parameters and neural dynamics for the GPe model given by Equations 11–14. We focus on parameters

**Table 1. Model parameters**

Parameter	Value	Reference	Parameter	Value
$\tau_p$	18.0 ms	Nambu and Llinas (1994)	$\Delta_p$	9.0
$\tau_a$	32.0 ms	Cooper and Stanford (2000)	$\Delta_a$	3.0
$\mu_{pp}, \mu_{aa}, \mu_{pa}, \mu_{ap}$	1.0 ms	Jaeger and Kita (2011)	$\eta_p$	12.0
$\sigma_{pp}, \sigma_{aa}, \sigma_{pa}, \sigma_{ap}$	0.6 ms	Jaeger and Kita (2011)	$\eta_a$	26.0
$\tau_r^{pp}, \tau_r^{aa}, \tau_r^{pa}, \tau_r^{ap}$	0.5 ms	Sims et al. (2008)	$J_{pp}$	15.0
$\tau_d^{pp}, \tau_d^{aa}, \tau_d^{pa}, \tau_d^{ap}$	5.0 ms	Sims et al. (2008)	$J_{ap}$	20.0
$r_e$	20.0 Hz	Wichmann and Soares (2006)	$J_{pa}$	5.0
$r_s$	2.0 Hz	Wichmann and Soares (2006)	$J_{aa}$	1.0
$J_{pe}$	50.0	Pamukcu et al. (2020)	$J_{ps}$	100.0
$J_{ae}$	15.0	Pamukcu et al. (2020)	$J_{as}$	10.0

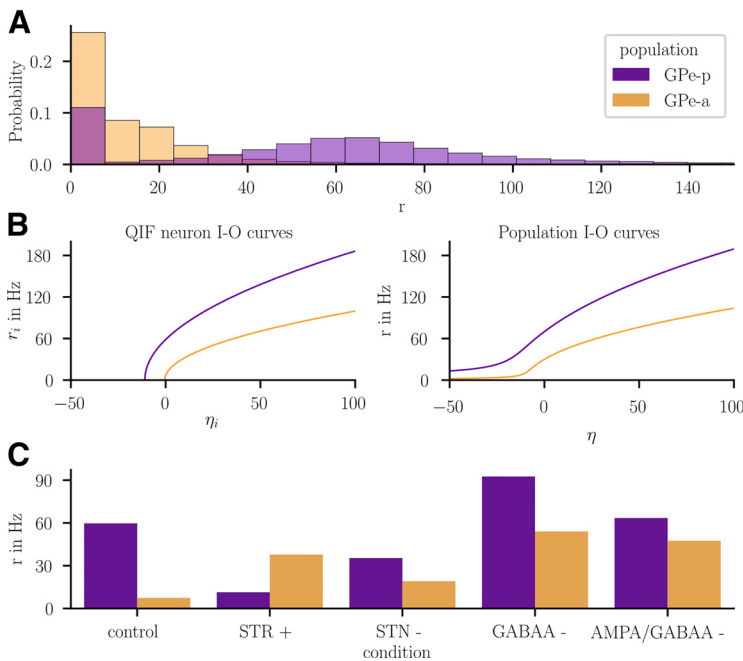


**Figure 1.** Configuration of the GPe model. **A**, Distributions of steady-state QIF firing rates under synaptic isolation, i.e., with  $J_{xy} = 0 \forall x, y \in \{p, a, e, s\}$ , for  $\eta_p = 11$  and  $\eta_a = 0.5$ . **B**, I-f curves for single GPe-p and GPe-a neurons (left) and the GPe-p and GPe-a populations (right) under synaptic isolation, i.e., with  $J_{xy} = 0 \forall x, y \in \{p, a, e, s\}$ . **C**, Steady-state average firing rates of GPe-p and GPe-a calculated from 1 s of model behavior under different conditions. (*control*) default parameters as reported in Table 1. (*STR +*) STR excitation, i.e.,  $r_s = 40$  Hz. (*STN -*) STN inhibition, i.e.,  $r_e = 2$  Hz. (*GABAA -*) blockade of GABAergic synaptic transmission, i.e.,  $J_{pp} = 1.5$ ,  $J_{ap} = 2.0$ ,  $J_{pa} = 0.5$ ,  $J_{aa} = 0.1$ ,  $J_{ps} = 10.0$ , and  $J_{as} = 1.0$ . (*AMPA/GABAA -*) blockade of all glutamatergic and GABAergic synaptic transmission, i.e.,  $J_{xy} = \frac{J_{xy}}{10} \forall x, y \in \{p, a, e, s\}$ , where  $J_{xy}^*$  represents the synaptic strengths used to calculate the firing rates.

that contribute to a difference between GPe-p and GPe-a, which include the coupling strengths within the GPe as well as additional inputs to the two populations. All coupling parameters are reported as  $k_{xy} = \frac{J_{xy}}{10}$  throughout this section.

### Effects of GPe-intrinsic coupling

As the first part of our analysis, we performed a bifurcation analysis of the GPe mean-field model given by Equations 11–14 to investigate whether different coupling patterns between prototypical (GPe-p) and arkyppallidal (GPe-a) cells promote different macroscopic states and phase transitions. We started out from the GPe coupling strengths listed in Table 1, which represent a coupling pattern where GPe-p inhibition of GPe-a is strongest and GPe-a axon collaterals are weaker than GPe-p axon collaterals, but still exist (for a comparison to experimental findings, see

Mallet et al., 2012; Ketzef and Silberberg, 2021). In this default state, input to the GPe populations led to changes in their firing rates but did not induce any phase transitions (Fig. 2A). Still, inhibition of GPe-p via decreases in  $\eta_p$  caused a fast increase in GPe-a firing rates. This interaction pattern between GPe-p and GPe-a changes when the intrinsic connections of the GPe are altered. As can be seen in Figure 2C, D, increases in  $k_{pp}$  lead to the emergence of a stable limit cycle via a supercritical Andronov-Hopf bifurcation. The emerging oscillations express a frequency in the  $\gamma$  range ( $\approx 50$ –60 Hz) and can be induced by changes in  $k_{pp}$  as well as changes in  $\eta_p$  (Fig. 2D,E). The Hopf curve in the  $\eta_p$ - $k_{pp}$  plane shows that this emergence of synchronized oscillations critically depends on  $k_{pp} > 0$  as well as

a sufficient excitatory drive as given by  $\eta_p > 0$ . We encountered a different phenomenon when increasing  $k_{pa}$ , the connection strength from GPe-a to GPe-p. For sufficient increases in  $k_{pa}$ , the system expresses twofold bifurcations that mark the outer boundaries of a bistable regime, in which transient inputs to GPe-p (or GPe-a) allow to switch between two stable states (Fig. 2F,H). One of those two stable states is a focus for which the GPe-p is in a high-activity regime and forces the GPe-a to a low-activity regime. The other stable state is also a focus where the GPe-a is in a high-activity regime and forces the GPe-p to a low-activity regime. These two stable equilibria are separated by a saddle focus. Thus, we found that strong bidirectional coupling between prototypical and arkyppallidal GPe populations allows for the existence of a bistable activity regime, where the two populations compete over a high-activity state. In Figure 2G, we show the curve of the fold bifurcations in the  $\eta_p$ - $k_{pa}$  plane, which collapse in a cusp bifurcation when  $k_{pa}$  becomes small. Furthermore, we find another Hopf curve that touches the fold curve at a zero-Hopf bifurcation. This Hopf curve covers a relatively small parameter range, however, and only appears on the lower branch within the bistable regime. The oscillations emerging from this limit cycle are small-amplitude  $\gamma$  oscillations.

As a next step, we investigated whether the frequency of the oscillations identified for increased self-inhibition of GPe-p critically depends on the axonal delays in our model, since estimates of these delays differ substantially in the literature (Jaeger and Kita, 2011; Ketzef and Silberberg, 2021). To this end, we simulated the behavior of our model for increasing values of  $\mu_{xy}$ ,  $\forall x, y \in \{p, a\}$ . As can be seen in Figure 3, increasing  $\mu_{xy}$  appears to drive the system over a Hopf bifurcation but does not affect the oscillation frequency in biologically plausible ranges.

### GPe response to periodic forcing

By now, we have established an understanding of the intrinsic, coupling-dependent GPe response to static, afferent inputs. We found that a dichotomous organization of the GPe with two distinct populations GPe-a and GPe-p results in coupling-dependent dynamic behavior that situates the GPe either near a bistable or near an oscillatory regime. These two different scenarios may

have substantially different consequences for the transmission and amplification of periodic input arriving at the GPe. Hence, as a next step, we analyzed the response of the GPe to periodic inputs when initialized in the bistable regime, in the oscillatory regime, or in the healthy steady-state regime. To this end, we applied periodic striatal input with period  $\omega$  and amplitude  $\alpha$  to the prototypical population. The bursting properties of striatal input were generated by applying a sigmoidal transformation to a Stuart-Landau oscillator (see Eqs. 17–20). In each regime, we performed numerical simulations of the model behavior for different values of  $\omega$  and  $\alpha$ . We then evaluated the average PAC between the phase of low-frequency signal components (2–30 Hz) and the amplitude of high-frequency signal components (50–250 Hz) of the GPe-p firing rate dynamics. Furthermore, we evaluated the PPC, that is, the phase dependency of the high-frequency components on the phase of the dominating low-frequency component. A detailed description of these measures is provided in Materials and Methods. As can be seen in Figure 4, we find that the GPe responds differently to periodic input depending on its dynamic regime.

In Figure 4A, the GPe response to periodic input is depicted for the default coupling pattern. In this case, a stable focus is the only equilibrium, and the input perturbs the system around that equilibrium at the input frequency. After a perturbation, the system relaxes back to the focus via damped oscillations. The amplitude of these oscillations scales with  $\alpha$ , as can be seen by comparing time series 1 and 2 of Figure 4A. Thus, stronger inputs generate stronger modulation of high-frequency amplitudes by low-frequency phases, resulting in increased PAC. Since the high-frequency focus dynamics are directly elicited by the low-frequency perturbations, increases in PAC always co-occur with increased PPC.

Figure 4B depicts the response of a bistable GPe to periodic input. In this regime, periodic inhibition forces the GPe-p toward the low-activity regime, if sufficiently strong (time series 1 and 2 of Fig. 4B for inputs that are too weak and sufficiently strong, respectively). If forced toward the low-activity regime, the GPe-p attempts to relax back to its natural high-activity regime (time series 2 and 4 of Fig. 4B). In this relaxation process, the system is affected by the strong focus dynamics of the saddle that separates the two stable states. For most combinations of  $\alpha$  and  $\omega$ ,

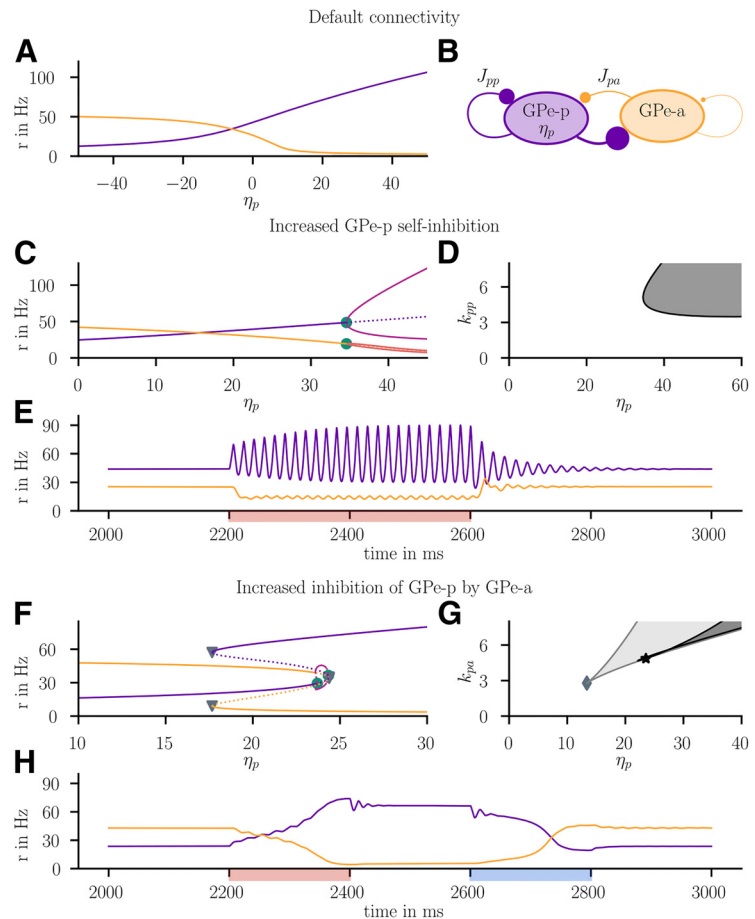


**Figure 2.** Phase transitions in the GPe. **A**, One-parameter bifurcation diagram varying the background input of GPe-p  $\eta_p$  for the default connectivity. **B**, Depiction of the GPe circuit and the bifurcation parameters. **C**, 1D parameter continuation in  $\eta_p$  for  $k_{pp} = 5$ . Green circles represent Andronov-Hopf bifurcations. Lines starting at the Hopf bifurcation indicate the minima and maxima of the emerging limit cycle. Solid (dotted) lines indicate stable (unstable) equilibria. **D**, 2D bifurcation diagram in  $\eta_p$  and  $k_{pp}$ . Black curve represents the continuation of the 1D Hopf bifurcation from **C** in the 2D parameter space. Shaded regions represent the parameter space where stable oscillations exist. **E**, GPe-p and GPe-a firing rates for  $k_{pp} = 5$  and  $\eta_p = 30$  show that additional input  $I_p(t) = 10.0$ , applied between  $2200 \leq t < 2600$ , forced the system over the Hopf bifurcation. **F**, 1D parameter continuation in  $\eta_p$  for  $k_{pa} = 5$ . Gray triangles represent fold bifurcations. **G**, 2D bifurcation diagram in  $\eta_p$  and  $k_{pa}$ . Gray rhombus represents a cusp bifurcation. Black star represents a zero-Hopf bifurcation. **H**, GPe-p and GPe-a firing rates for  $k_{pa} = 5$  and  $\eta_p = 21.0$  show switching between the two stable branches via  $I_p(t) = 5$  applied between  $2200 \leq t < 2400$  and  $I_p(t) = -5$  applied between  $2600 \leq t < 2800$ .

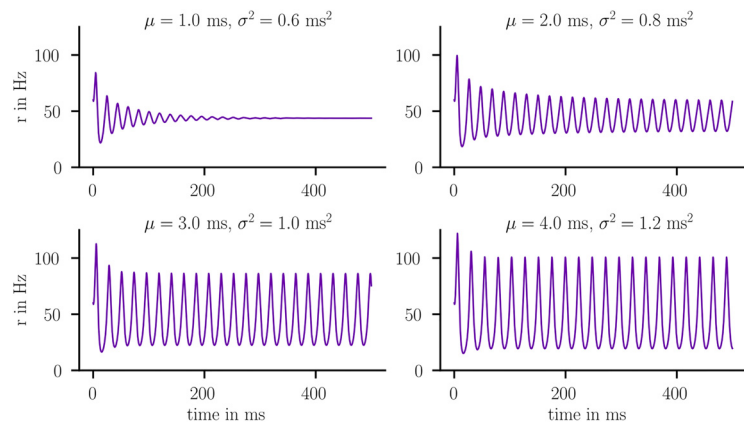


**Figure 3.** Effect of increasing axonal delays on GPe oscillations. Time series represent average firing rates of GPe-p, abbreviated as  $r$ . Reported values of  $\mu$  and  $\sigma$  refer to changes the parameter  $\mu_{xy}$  and  $\sigma_{xy}$ ,  $\forall x, y \in \{p, a\}$ .

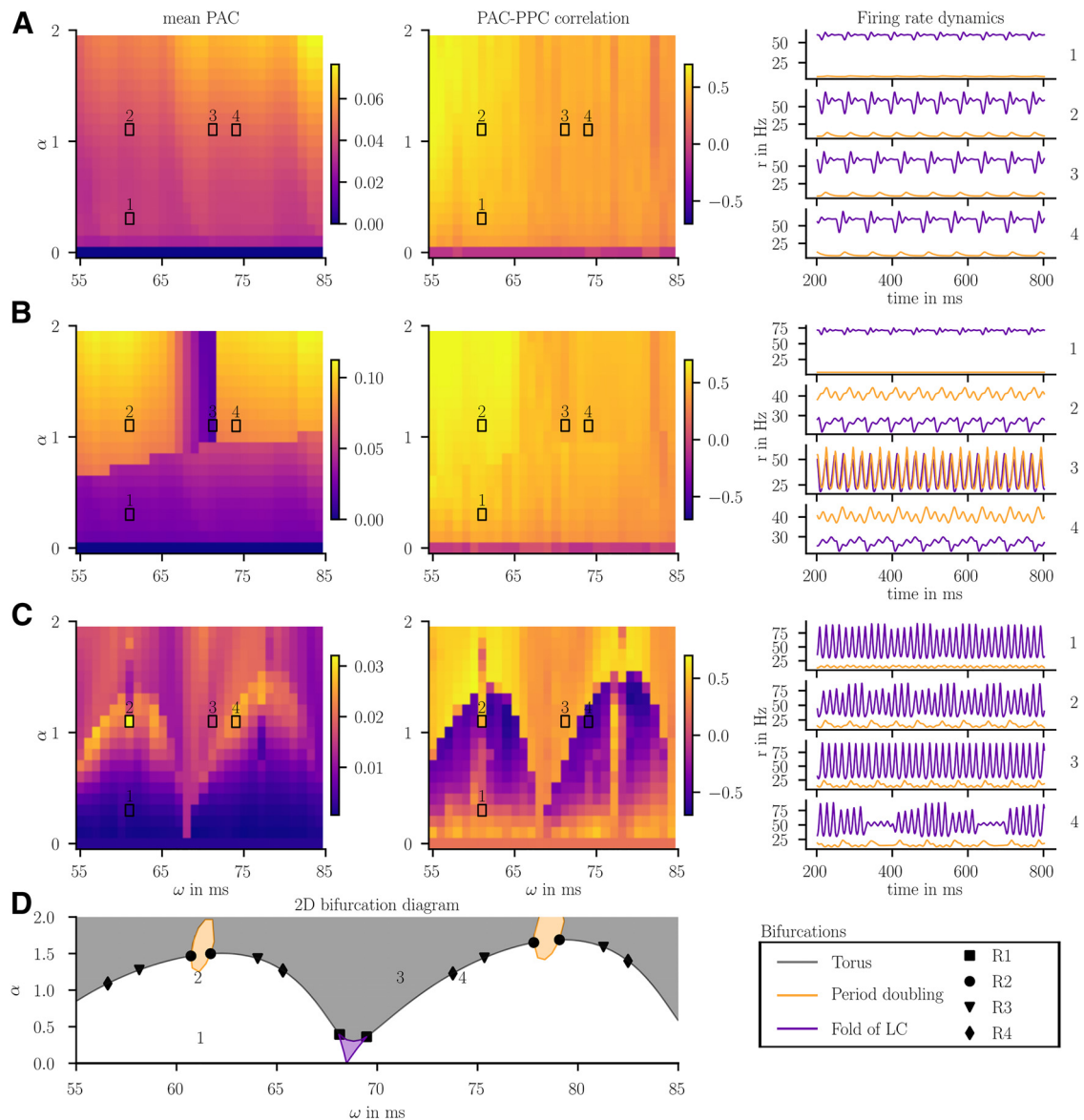


**Figure 4.** PAC and PPC in the periodically inhibited GPe. The input  $i_p(t)$  was applied with different frequencies  $\frac{1}{\omega}$  and amplitudes  $\alpha$ . For each input, the mean PAC between phases of low-frequency components (2–30 Hz) and amplitudes of high-frequency components (50–250 Hz) of the GPe-p firing rate was calculated. Furthermore, the correlation between PAC and PPC values was evaluated across all pairs of low- and high-frequency components. Exemplary time series are provided for GPe-p (purple) and GPe-a (orange) firing rates of four different inputs: (1)  $\omega = 61$  ms,  $\alpha = 0.3$ ; (2)  $\omega = 61$  ms,  $\alpha = 1.1$ ; (3)  $\omega = 71$  ms,  $\alpha = 1.1$ ; and (4)  $\omega = 74$  ms,  $\alpha = 1.1$ . **A**, Results for default parameters. **B**, Results for  $k_{pp} = 50$  and  $\eta_p = 24$ . **C**, Results for  $k_{pp} = 50$  and  $\eta_p = 40$ . **D**, 2D Bifurcation diagram in the  $\alpha$  –  $\omega$  plane, which shows emergence of resonant behavior and period doubling of GPe oscillations along a torus bifurcation curve.

this behavior creates oscillations with interleaved large- and small-amplitude oscillations, where the large-amplitude oscillations act as an amplification of the low-frequency input and cause cross-frequency coupling with the high-frequency, small-amplitude focus dynamics. Stronger inputs generate stronger modulation of high-frequency amplitudes by low-frequency phases, as evaluated by PAC. Such increases in PAC occur together with increased phase locking between low- and high-frequency components. This can be observed by the generally high PAC-PPC correlations in Figure 4B. Interestingly, there also exists a relatively narrow window in  $\omega$ , where the periodic inhibition of the GPe-p forces the system to stay within the domain of influence of the unstable saddle focus, thus causing periodic oscillations with strongly reduced PAC (see time series 3 of Fig. 4B).

More complex, resonant behavior can arise for periodic forcing of the GPe, if the GPe already expresses oscillations autonomously (Fig. 4C,D). When increasing  $\alpha$ , the system undergoes a

torus bifurcation that emerges from the interaction between the intrinsic limit cycle and the extrinsic, periodic input. As can be seen from the firing rate dynamics in Figure 4C, strong amplitude modulations of the intrinsic limit cycle exist in the vicinity of this torus bifurcation. A continuation of the torus bifurcation in the  $\omega$ – $\alpha$  plane reveals that the system expresses various resonances of the intrinsic limit cycle with the extrinsic input. Close to regimes of 1:2 resonances, we were able to identify small loci of period doubling bifurcations, suggesting the existence of chaotic regimes. These bifurcations are also reflected in the PAC and PPC profiles of the system. PAC values are low before the system undergoes the torus bifurcation and increase near and after the torus bifurcation. In the vicinity of the torus bifurcation, we find regimes where strong PAC can coexist with low PPC values. These regions express negative correlations between PAC and PPC and are clearly separated from regions where increased PAC and PPC coexist (Fig. 4C).

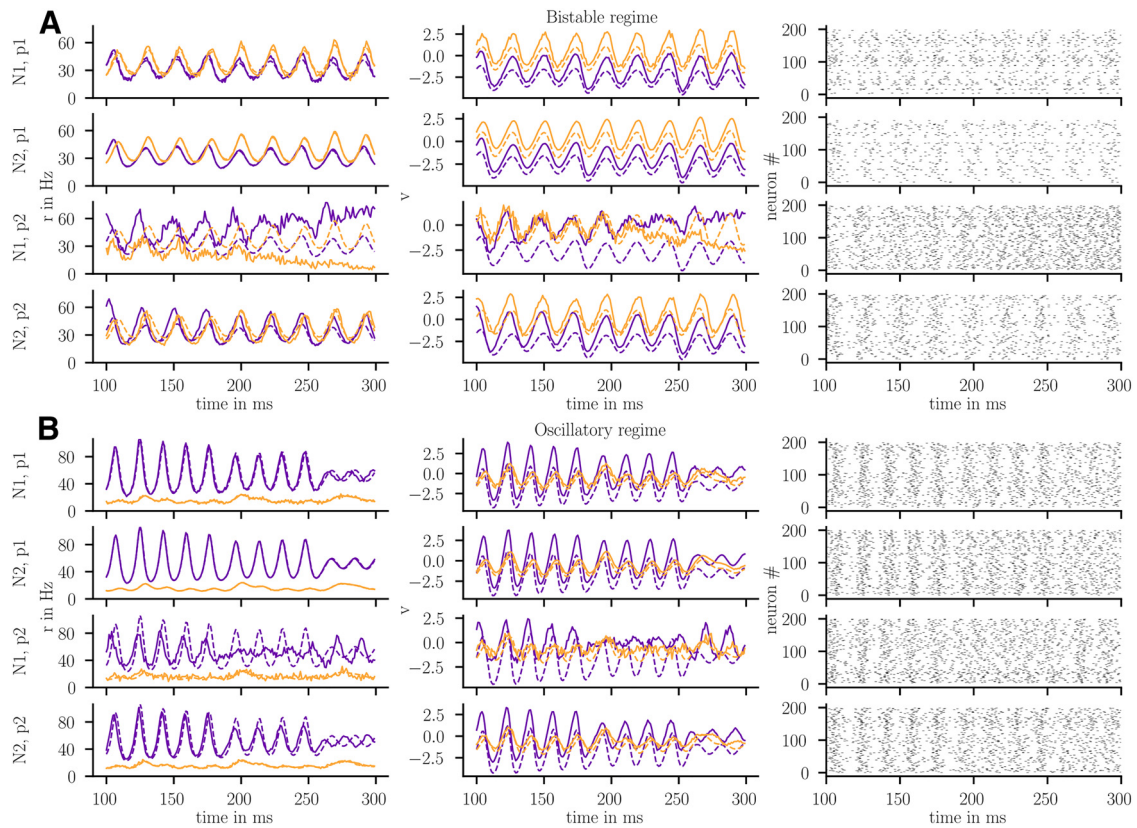


**Figure 5.** Comparison between mean-field model (dashed lines) and spiking neural networks (SNNs) under periodic stimulation. The first and second columns represent the average firing rate and average membrane potential across the population, whereas the last column represents spike timings from 200 randomly chosen neurons of the population. SNNs are composed of  $N_p = 4N_{1/2}$  GPe-p and  $N_a = 2N_{1/2}$  GPe-a neurons, where  $N_1 = 1000$  and  $N_2 = 10,000$ . From all possible synaptic connections in the SNN, either  $p_1 = 100\%$  or  $p_2 = 5\%$  is established. **A**, Results for  $k_{pp} = 5$ ,  $\eta_p = 24$ ,  $\alpha = 1.1$ , and  $\omega = 71$ . **B**, Results for  $k_{pp} = 5$ ,  $\eta_p = 40$ ,  $\alpha = 1.1$ , and  $\omega = 74$ .

### Model generalization to GPe spiking neural networks

In this section, we report how the above-described findings generalize to spiking neural networks (SNNs) of coupled GPe-p and GPe-a cells with realistic cell counts and coupling probabilities. To this end, we attempted to replicate the mean-field model dynamics shown in time series 3 of Figure 4B and time series 4 of Figure 4C and in SNNs with (1) different network sizes and (2) different coupling probabilities. We created a total of four SNNs with (1) either all-to-all coupling or only 5% of all possible connections, and (2) either  $N_p = 4000$  ( $N_a = 2000$ ) GPe-p (GPe-a) cells or  $N_p = 40,000$  ( $N_a = 20,000$ ) GPe-p (GPe-a) cells. We then repeated our simulations of the GPe response to periodic stimulation for spiking neural networks initialized near the bistable and in the oscillatory regime (same parameterizations as reported in Fig. 4 for the mean-field model). The dynamics of all four SNNs can be seen compared with the mean-field predictions in Figure 5. As expected, we find that an all-to-all coupled SNN of large size behaves nearly identical to the mean-field prediction, where the remaining difference in the oscillation amplitude is an effect of the network size and would vanish if we increased the network size even further (see difference between SNNs with  $N_1$  and  $N_2$ ). Interestingly, we find that reducing the number of synaptic connections to  $p = 5\%$  of all possible connections attenuates synchronized oscillations in the network for small network sizes. However, for a sufficiently large network, the SNN follows the macroscopic dynamics predicted by the mean-field model, even when  $p = 5\%$ . This holds for both the bistable as well as the oscillatory regime.

### Discussion

In this work, we investigated the implications of a dichotomous GPe structure on its intrinsic dynamic regimes and on its response to oscillatory input. This was motivated by experimental results that strongly suggest that there exist two neuron types (GPe-p and GPe-a) inside GPe with different projection targets and electrophysiological features (Mallet et al., 2012; Abdi et al., 2015; Hernández et al., 2015; Hegeman et al., 2016). Our investigations were based on populations of coupled QIF neurons, for which we derived exact mean-field equations describing the low-dimensional dynamics of average membrane potentials and firing rates. This two-population model was set up such that it accounts for the I-f curves of GPe-p and GPe-a cells (Abdi et al., 2015), firing rate heterogeneity inside each population (Migueluez et al., 2012; Aristieta et al., 2021; Ketzef and Silberberg, 2021), as well as the response of GPe-p and GPe-a to extrinsic stimulation (Kita et al., 2004; Aristieta et al., 2021). Next, we investigated the dependence of the macroscopic neurodynamics of this model on the underlying connectivity between GPe-p and GPe-a. We found that strong GPe-p projections and weak GPe-a projections produced realistic steady-state firing rates ( $r_p \approx 60$  Hz and  $r_a \approx 10$  Hz) and responses to STR and STN stimulation (Kita et al., 2004; Dodson et al., 2015; Aristieta et al., 2021). In this regime, the model was relatively robust to changes in its extrinsic input. While alterations of the background input led to changes in the average firing rates, they were not sufficient to induce phase transitions in the model.

Under dopamine depletion, GABAergic postsynaptic currents of GPe-to-GPe synapses have been reported to increase in



strength (Migueluez et al., 2012). However, it is unclear which GPe-to-GPe synapses are affected by this and how these changes may influence GPe dynamics. Thus, we investigated whether increases in the strength of specific GPe connections induce changes in the behavior of the system. To this end, we focused on the synapses inhibiting the GPe-p, since increased inhibition of GPe-a would merely reduce its already low steady-state firing rates and, hence, not induce any phase transitions to the GPe dynamics.

When the strength of GPe-p inhibition by GPe-a was increased, we found that a bistable regime emerged in which GPe-p and GPe-a competed over a high-activity state. This regime could provide a form of network memory and a reliable way to switch GPe output between the different projection targets of GPe-p (STN) and GPe-a (STR). Furthermore, if the GPe was situated in the bistable regime, periodic inputs from STR were amplified because of the existence of two different attracting states. Indeed, when we applied periodic input from STR to GPe-p in the  $\beta$  frequency range characteristic for PD (Brown, 2003; Hammond et al., 2007), the GPe-p was periodically forced from a high-activity state down to a low-activity state, thus resonating at the input frequency. Importantly, this led to strong phase-amplitude as well as PPC between  $\beta$  and  $\gamma$  components of the GPe-p firing rate dynamics. Interestingly, the synchronized neural activity that has been detected in recordings of STN and GPe activity from PD patients expressed not only increased power in the  $\beta$  frequency band, but also increased PAC between the phase of  $\beta$  components and the amplitude of  $\gamma$  components (López-Azcárate et al., 2010). Our model can explain these findings as follows: dopamine depletion at the GPe leads to an increased strength of GPe-a to GPe-p synapses in PD (Migueluez et al., 2012). This structural change moves the system closer to a bistable regime. By moving closer to the boundaries of the bistable regime, oscillatory inputs from STN or STR become more likely to elicit switching between the two stable states of the GPe. At both of these input sites, increased  $\beta$  oscillations have been reported in PD (Brown, 2003; Belluscio et al., 2014). Periodic forcing of the bistable GPe would then perturb the system in a phase space controlled by multiple stable and unstable foci with focus frequencies in the  $\gamma$  range, thus causing damped  $\gamma$  oscillations with input-triggered amplitude modulations. Hence, in this scenario, PD-related intrinsic changes can cause increased susceptibility of the GPe to periodic inputs, but not autonomous GPe oscillations.

When we instead increased the GPe-p to GPe-p self-inhibition, we found that stable oscillations in a  $\gamma$  frequency range ( $\approx 50$ – $60$  Hz) could emerge. These oscillations were driven by the dynamic interactions between the pace-making properties of the GPe-p and its delayed self-inhibition. Most likely, these oscillations reflect the same synchronization mechanism as reported for a single population with delayed self-inhibition (Luccioli et al., 2019). According to their results, oscillations are counteracted by neural heterogeneity. This way, our results can be linked to the considerations in (Wilson, 2013), which suggest that strong firing rate heterogeneity together with recurrent inhibition inside GPe may serve to desynchronize GPe activity under healthy conditions. In accordance with experimental data, we modeled the GPe-p with highly heterogeneous single-cell firing rates (Migueluez et al., 2012; Hernández et al., 2015; Aristieta et al., 2021; Ketzef and Silberberg, 2021). This way, inhibitory feedback from the GPe-p provides the means to suppress synchronized oscillations inside the GPe, which supports these considerations. Experimental evidence from animal models of

PD suggest that GPe activity shows increased synchronization in PD (Wichmann and Soares, 2006; Mallet et al., 2012). Our model can explain these findings as follows: dopamine depletion causes the strength of GPe-p self-inhibition to increase in PD (Migueluez et al., 2012). This moves the GPe system closer to or even across the boundaries of an oscillatory regime. The emerging limit cycle leads to narrow-band  $\gamma$  oscillations and thus cannot explain the emergence of  $\beta$  oscillations in the parkinsonian BG (Brown, 2003; Hammond et al., 2007). However, assuming that burst-like afferent inputs drive the GPe at a  $\beta$  frequency, our findings predict that GPe-intrinsic  $\gamma$  oscillations can resonate with the input, leading to a waxing and waning of the  $\gamma$  oscillations. Such waxing-and-waning behavior also implicates increased PAC, which may occur together with decreased PPC, according to our simulations. The latter finding was unique for the oscillatory regime of the GPe. Similarly, complex patterns of cross-frequency coupling have been reported previously in an instantaneously coupled two-population QIF model with sinusoidal forcing in the  $\alpha$  frequency range (10 Hz) (Ceni et al., 2020). Thus, our results show under which conditions the GPe system can express the characteristic dynamics that have been identified in more abstract models of two populations with mutual inhibition.

The mathematical model presented in this paper can serve as a basis for future BG models. We have shown that a mean-field model derived under the assumptions of all-to-all coupling and an infinite number of neurons accurately describes the dynamics of a SNN with realistic cell counts and coupling densities (Hegeman et al., 2016). Thus, our model lends itself to multiscale approaches. It can easily be extended by additional biological details, such as plasticity mechanisms (Gast et al., 2020) or gap junctions (Pietras et al., 2019). The latter may be of particular interest to investigate parkinsonian conditions inside the GPe (Schwab et al., 2014). Furthermore, our model can be used as a basis for experimental investigations of GPe structure-function relationships in healthy and diseased states. First, the I-f curves reported at the single-cell and population level allow a comparison of our model with experimental data on the input-output relationship of GPe cells. Second, our model predicts specific phase transitions of GPe dynamics to emerge for increased strengths of GPe-p to GPe-p or GPe-a to GPe-p synapses. Experimental investigation of the GPe response to GPe-p stimulation under dopamine-depleted conditions could serve to infer whether GPe dopamine depletion increases these synaptic strengths sufficiently to induce these phase transitions. Finally, our results indicate that the GPe expresses distinct responses to periodic input from STR, based on its dynamic regime. Specifically, PAC and PPC profiles of GPe firing rates can distinguish between the healthy steady-state regime, the bistable regime, and the oscillatory regime of the periodically forced GPe. Thus, extrinsic periodic stimulation of indirect pathway STR projection neurons could be used in combination with measurements of PAC and PPC of GPe firing rates to infer the underlying dynamic regime and synaptic connectivity of the GPe in healthy versus diseased states.

## References

- Abdi A, Mallet N, Mohamed FY, Sharott A, Dodson PD, Nakamura KC, Suri S, Avery SV, Larvin JT, Garas FN, Garas SN, Vinciati F, Morin S, Bezard E, Baufreton J, Magill PJ (2015) Prototypic and arkiypallidal neurons in the dopamine-intact external globus pallidus. *J Neurosci* 35:6667–6688.
- Abraham KP, Chancey JH, Chan CS, Lovinger DM (2017) Ethanol-sensitive pacemaker neurons in the mouse external globus pallidus. *Neuropsychopharmacology* 42:1070–1081.

- Alexander G, Crutcher M (1990) Functional architecture of basal ganglia circuits: neural substrates of parallel processing. *Trends Neurosci* 13:266–271.
- Aristieta A, Barresi M, Azizpour Lindi S, Barrière G, Courtand G, de la Crompe B, Guilhemsang L, Gauthier S, Fioramonti S, Baufreton J, Mallet NP (2021) A disynaptic circuit in the globus pallidus controls locomotion inhibition. *Curr Biol* 31:707–721.e7.
- Belluscio MA, Escande MV, Keifman E, Riquelme LA, Murer MG, Zold CL (2014) Oscillations in the basal ganglia in Parkinson's disease: role of the striatum. *Basal Ganglia* 3:203–212.
- Bolam JP, Hanley JJ, Booth PA, Bevan MD (2000) Synaptic organisation of the basal ganglia. *J Anat* 196:527–542.
- Brown P (2003) Oscillatory nature of human basal ganglia activity: relationship to the pathophysiology of Parkinson's disease. *Mov Disord* 18:357–363.
- Ceni A, Olmi S, Torcini A, Angulo-Garcia D (2020) Cross frequency coupling in next generation inhibitory neural mass models. *Chaos* 30:053121.
- Cooper AJ, Stanford IM (2000) Electrophysiological and morphological characteristics of three subtypes of rat globus pallidus neurone in vitro. *J Physiol* 527:291–304.
- Corbit VL, Whalen TC, Zitelli KT, Crilly SY, Rubin JE, Gittis AH (2016) Pallidostriatal projections promote  $\beta$  oscillations in a dopamine-depleted biophysical network model. *J Neurosci* 36:5556–5571.
- Deco G, Jirsa VK, Robinson PA, Breakspear M, Friston K (2008) The dynamic brain: from spiking neurons to neural masses and cortical fields. *PLoS Comput Biol* 4:e1000092.
- DeLong MR (1971) Activity of pallidal neurons during movement. *J Neurophysiol* 34:414–427.
- Dodson PD, Larvin JT, Duffell JM, Garas FN, Doig NM, Kessaris N, Duguid IC, Bogacz R, Butt SJ, Magill PJ (2015) Distinct developmental origins manifest in the specialized encoding of movement by adult neurons of the external globus pallidus. *Neuron* 86:501–513.
- Doedel EJ, Fairgrieve TF, Sandstede B, Champneys AR, Kuznetsov YA, Wang X (2007) AUTO-07P: continuation and bifurcation software for ordinary differential equations. Technical report.
- Dumont G, Gutkin B (2019) Macroscopic phase resetting-curves determine oscillatory coherence and signal transfer in inter-coupled neural circuits. *PLoS Comput Biol* 15:e1007019.
- Fujimura K (1997) Centre manifold reduction and the Stuart-Landau equation for fluid motions. *Proc R Soc Lond A* 453:181–203.
- Fujita T, Fukai T, Kitano K (2012) Influences of membrane properties on phase response curve and synchronization stability in a model globus pallidus neuron. *J Comput Neurosci* 32:539–553.
- Fujiyama F, Nakano T, Matsuda W, Furuta T, Udagawa J, Kaneko T (2016) A single-neuron tracing study of arky pallidal and prototypic neurons in healthy rats. *Brain Struct Funct* 221:4733–4740.
- Gast R, Rose D, Salomon C, Möller HE, Weiskopf N, Knösche TR (2019) PyRates: a Python framework for rate-based neural simulations. *PLoS One* 14:e0225900.
- Gast R, Schmidt H, Knösche TR (2020) A mean-field description of bursting dynamics in spiking neural networks with short-term adaptation. *Neural Comput* 32:1615–1634.
- Gong R, Wegscheider M, Mühlberg C, Gast R, Fricke C, Rumpf JJ, Nikulin VV, Knösche TR, Classen J (2021) Spatiotemporal features of beta-gamma phase-amplitude coupling in Parkinson's disease derived from scalp EEG. *Brain* 144:487–503.
- Gutkin BS, Ermentrout GB, Reyes AD (2005) Phase-response curves give the responses of neurons to transient inputs. *J Neurophysiol* 94:1623–1635.
- Günay C, Edgerton JR, Jaeger D (2008) Channel density distributions explain spiking variability in the globus pallidus: a combined physiology and computer simulation database approach. *J Neurosci* 28:7476–7491.
- Hammond C, Bergman H, Brown P (2007) Pathological synchronization in Parkinson's disease: networks, models and treatments. *Trends Neurosci* 30:357–364.
- Hegeman DJ, Hong ES, Hernández VM, Chan CS (2016) The external globus pallidus: progress and perspectives. *Eur J Neurosci* 43:1239–1265.
- Hernández VM, Hegeman DJ, Cui Q, Kelver DA, Fiske MP, Glajch KE, Pitt JE, Huang TY, Justice NJ, Chan CS (2015) Parvalbumin<sup>+</sup> neurons and Npas1<sup>+</sup> neurons are distinct neuron classes in the mouse external globus pallidus. *J Neurosci* 35:11830–11847.
- Higgs MH, Jones JA, Chan CS, Wilson CJ (2021) Periodic unitary synaptic currents in the mouse globus pallidus during spontaneous firing in slices. *J Neurophysiol* 125:1482–1500.
- Izhikevich EM (2000) Neural excitability, spiking and bursting. *Int J Bifurcation Chaos* 10:1171–1266.
- Jaeger D, Kita H (2011) Functional connectivity and integrative properties of globus pallidus neurons. *Neuroscience* 198:44–53.
- Jaeger D, Gilman S, Aldridge JW (1995) Neuronal activity in the striatum and pallidum of primates related to the execution of externally cued reaching movements. *Brain Res* 694:111–127.
- Je, drzejewski-Szmek Z, Abrahao KP, Je, drzejewska-Szmek J, Lovinger DM, Blackwell KT (2018) Parameter optimization using Covariance Matrix Adaptation—Evolutionary Strategy (CMA-ES), an approach to investigate differences in channel properties between neuron subtypes. *Front Neuroinform* 12:47.
- Jenkinson N, Kühn AA, Brown P (2013) Gamma oscillations in the human basal ganglia. *Exp Neurol* 245:72–76.
- Ketzel M, Silberberg G (2021) Differential synaptic input to external globus pallidus neuronal subpopulations in vivo. *Neuron* 109:516–529.e4.
- Kita H (2007) Globus pallidus external segment. *Prog Brain Res* 160:111–133.
- Kita H, Nambu A, Kaneda K, Tachibana Y, Takada M (2004) Role of ionotropic glutamatergic and GABAergic inputs on the firing activity of neurons in the external pallidum in awake monkeys. *J Neurophysiol* 92:3069–3084.
- Kuznetsov YA (2004) Elements of applied bifurcation theory, Ed 3. New York: Springer.
- Lofredi R, Neumann WJ, Brücke C, Huebl J, Krauss JK, Schneider GH, Kühn AA (2019) Pallidal beta bursts in Parkinson's disease and dystonia. *Mov Disord* 34:420–424.
- Lourens MA, Schwab BC, Nirody JA, Meijer HG, van Gils SA (2015) Exploiting pallidal plasticity for stimulation in Parkinson's disease. *J Neural Eng* 12:026005.
- Luccioli S, Angulo-García D, Torcini A (2019) Neural activity of heterogeneous inhibitory spiking networks with delay. *Phys Rev E* 99:052412.
- Luke TB, Barreto E, So P (2013) Complete classification of the macroscopic behavior of a heterogeneous network of theta neurons. *Neural Comput* 25:3207–3234.
- López-Azcárate J, Tainta M, Rodríguez-Oroz MC, Valencia M, González R, Guridi J, Iriarte J, Obeso JA, Artieda J, Alegre M (2010) Coupling between beta and high-frequency activity in the human subthalamic nucleus may be a pathophysiological mechanism in Parkinson's disease. *J Neurosci* 30:6667–6677.
- Mallet N, Pogosyan A, Márton LF, Bolam JP, Brown P, Magill PJ (2008) Parkinsonian beta oscillations in the external globus pallidus and their relationship with subthalamic nucleus activity. *J Neurosci* 28:14245–14258.
- Mallet N, Micklem B, Henny P, Brown M, Williams C, Bolam JP, Nakamura K, Magill P (2012) Dichotomous organization of the external globus pallidus. *Neuron* 74:1075–1086.
- Meijer HG, Dercole F, Oldeman B (2009) Numerical bifurcation analysis. In: *Encyclopedia of complexity and systems science*, pp 6329–6352. New York: Springer.
- Mercer JN, Chan CS, Tkatch T, Held J, Surmeier DJ (2007) Nav1.6 sodium channels are critical to pacemaking and fast spiking in globus pallidus neurons. *J Neurosci* 27:13552–13566.
- Migueluez C, Morin S, Martinez A, Goillandeau M, Bezard E, Bioulac B, Baufreton J (2012) Altered pallido-pallidal synaptic transmission leads to aberrant firing of globus pallidus neurons in a rat model of Parkinson's disease. *J Physiol* 590:5861–5875.
- Montbrío E, Pázó D, Roxin A (2015) Macroscopic description for networks of spiking neurons. *Phys Rev X* 5:021028.
- Nambu A, Llinas R (1994) Electrophysiology of globus pallidus neurons in vitro. *J Neurophysiol* 72:1127–1139.
- Nevedo-Holgado AJ, Mallet N, Magill PJ, Bogacz R (2014) Effective connectivity of the subthalamic nucleus–globus pallidus network during Parkinsonian oscillations. *J Physiol* 592:1429–1455.
- Pamukcu A, Cui Q, Xenias HS, Berceau BL, Augustine EC, Fan I, Chalasani S, Hantman AW, Lerner TN, Boca SM, Chan CS (2020) Parvalbumin<sup>+</sup> and Npas1<sup>+</sup> pallidal neurons have distinct circuit topology and function. *J Neurosci* 40:7855–7876.

- Pavlidis A, Hogan SJ, Bogacz R (2015) Computational models describing possible mechanisms for generation of excessive beta oscillations in Parkinson's disease. *PLoS Comput Biol* 11:e1004609.
- Pietras B, Devalle F, Roxin A, Daffertshofer A, Montbrío E (2019) Exact firing rate model reveals the differential effects of chemical versus electrical synapses in spiking networks. *Phys Rev E* 100:042412.
- Rubin JE (2017) Computational models of basal ganglia dysfunction: the dynamics is in the details. *Curr Opin Neurobiol* 46:127–135.
- Schmidt H, Avitabile D, Montbrío E, Roxin A (2018) Network mechanisms underlying the role of oscillations in cognitive tasks. *PLoS Comput Biol* 14:e1006430.
- Schmidt H, Knösche TR (2019) Action potential propagation and synchronization in myelinated axons. *PLoS Comput Biol* 15:e1007004.
- Schroll H, Hamker FH (2016) Basal ganglia dysfunctions in movement disorders: what can be learned from computational simulations. *Mov Disord* 31:1591–1601.
- Schultheiss NW, Edgerton JR, Jaeger D (2010) Phase response curve analysis of a full morphological globus pallidus neuron model reveals distinct perisomatic and dendritic modes of synaptic integration. *J Neurosci* 30:2767–2782.
- Schwab BC, Heida T, Zhao Y, van Gils SA, van Wezel RJ (2014) Pallidal gap junctions: triggers of synchrony in Parkinson's disease? *Mov Disord* 29:1486–1494.
- Sims RE, Woodhall GL, Wilson CL, Stanford IM (2008) Functional characterization of GABAergic pallidopallidal and striatopallidal synapses in the rat globus pallidus in vitro. *Eur J Neurosci* 28:2401–2408.
- Smith H (2011) Distributed delay equations and the linear chain trick. In: *An introduction to delay differential equations with applications to the life sciences*, Texts in applied mathematics, pp 119–130. New York: Springer.
- Tort AB, Komorowski R, Eichenbaum H, Kopell N (2010) Measuring phase-amplitude coupling between neuronal oscillations of different frequencies. *J Neurophysiol* 104:1195–1210.
- Virtanen P, Gommers R, Oliphant TE, Haberland M, Reddy T, Cournapeau D, Burovski E, Peterson P, Weckesser W, Bright J, van der Walt SJ, Brett M, Wilson J, Millman KJ, Mayorov N, Nelson AR, Jones E, Kern R, Larson E, Carey CJ, et al. (2020) SciPy 1.0: fundamental algorithms for scientific computing in Python. *Nat Methods* 17:261–272.
- Wichmann T (2019) Changing views of the pathophysiology of Parkinsonism. *Mov Disord* 34:1130–1143.
- Wichmann T, Soares J (2006) Neuronal firing before and after burst discharges in the monkey basal ganglia is predictably patterned in the normal state and altered in Parkinsonism. *J Neurophysiol* 95:2120–2133.
- Wilson CJ (2013) Active decorrelation in the basal ganglia. *Neuroscience* 250:467–482.